



Published in final edited form as:

Mol Genet Metab. 2009 March ; 96(3): 133–144. doi:10.1016/j.ymgme.2008.11.164.

Retained Features of Embryonic Metabolism in the Adult MRL Mouse

Robert K. Naviaux^{1,*}, Thuy P. Le¹, Khamillia Bedelbaeva², John Leferovich², Dmitri Gourevitch², Pawel Sachdyn², Xiang-Ming Zhang², Lise Clark², and Ellen Heber-Katz^{2,*}

¹The Mitochondrial and Metabolic Disease Center, Departments of Medicine and Pediatrics University of California, San Diego, CA

²The Wistar Institute, Philadelphia, PA

Abstract

The MRL mouse is an inbred laboratory strain that was derived by selective breeding in 1960 from the rapidly growing LG/J (Large) strain. MRL mice grow to nearly twice the size of other commonly used mouse strains, display uncommonly robust healing and regeneration properties, and express later onset autoimmune traits similar to Systemic Lupus Erythematosus. The regeneration trait (*heal*) in the MRL mouse maps to 14–20 quantitative trait loci and the autoimmune traits map to 5–8 loci. In this paper we report the metabolic and biochemical features that characterize the adult MRL mouse and distinguish it from C57BL/6 control animals. We found that adult MRL mice have retained a number of features of embryonic metabolism that are normally lost during development in other strains. These include an emphasis on aerobic glycolytic energy metabolism, increased glutamate oxidation, and a reduced capacity for fatty acid oxidation. MRL tissues, including the heart, liver, and regenerating ear hole margins, showed considerable mitochondrial genetic and physiologic reserve, decreased mitochondrial transmembrane potential ($\Delta\Psi_m$), decreased reactive oxygen species (ROS), and decreased oxidative phosphorylation, yet increased mitochondrial DNA and protein content. The discovery of embryonic metabolic features led us to look for cells that express markers of embryonic stem cells. We found that the adult MRL mouse has retained populations of cells that express the stem cell markers *Nanog*, *Islet-1*, and *Sox2*. These are present in the heart at baseline and highly induced after myocardial injury. The retention of embryonic features of metabolism in adulthood is rare in mammals. The MRL mouse provides a unique experimental window into the relationship between metabolism, stem cell biology, and regeneration.

Keywords

mitochondria; oxidative phosphorylation; mammalian tissue regeneration; aerobic glycolysis; adult stem cells; metabolic neoteny

*Communicating Authors: RKN, Naviaux@ucsd.edu, phone: 619-543-2904, fax: 619-543-7868; EH-K, heberkatz@wistar.org, phone: 215-898-3710, fax: 215-898-3868.

Author Contributions

RKN and EH-K conceived the experiments and wrote the paper. RKN and TPL performed the mitochondrial experiments. JL did the myocardial injuries. LC did the ear punch studies. DG and X-MZ did the western blots. KB and DG did the immunofluorescence and immunohistochemistry and generated the primary fibroblast cultures. PS did the glutathione determinations.

Competing Financial Interests

The authors declare they have no financial or non-financial conflicts of interest.

INTRODUCTION

Unlike other strains of mice, MRL mice are capable of complete closure of a through-and-through hole punch in ear pinnae [1] and virtual complete restoration of right ventricular myocardium structure and function following a cryoinjury [2]. In addition, a regeneration-specific blastema, comprised of a self-organizing region of proliferating progenitor cells of mesenchymal origin [3,4], develops at the margin of tissue injury in MRL mice [5,6]. The ear hole closure or *heal* phenotype of the MRL mouse is multigenic, with at least 14–20 quantitative trait loci (QTLs) that contribute to the phenotype [7,8]. In addition to the remarkable regenerative characteristics of the MRL mouse that have been studied in young adults in the first 2–6 months of life, older animals develop an autoimmune disease similar to Systemic Lupus Erythematosus [9]. Autoantibodies to double strand DNA are detectable at 6 months, and immune complex-associated glomerulonephritis and vasculitic skin lesions are apparent after 12 months of age. The autoimmune traits have been mapped to 5–8 loci on mouse chromosomes 1, 4, and 5 [9,10]. Age-related hearing loss also occurs by about 6 months of age, but the genes responsible for hearing loss in the MRL have not yet been mapped [11,12]. Age-related hearing loss in the A/J mouse strain has been mapped to two loci, a nuclear gene on chromosome 10 and a mitochondrial DNA (mtDNA) gene shown to have an insertion of an adenosine in the poly(A) tract of the mitochondrial arginyl-tRNA [13]. Interestingly, the mtDNA of the MRL mouse was recently found to be heteroplasmic for insertions in the poly(A) tract of the arginyl-tRNA and for a T3900C substitution in the methionyl-tRNA (14). Mitochondrial methionyl-tRNA is exported into the cytoplasm where it plays a role in RNA silencing by interaction with Argonaute 2 (*Ago2*), the catalytic core of the RNA-induced silencing complex (RISC) [15]. The relationship of improved healing and age-related autoimmunity to the mitochondrial DNA abnormalities in the MRL mouse remains unknown [14]. In this paper, we focus on the mitochondrial and metabolic characteristics of the MRL mouse and show that these features sharply distinguish the MRL mouse from the non-healer, standard control strain, C57BL/6 (B6). Our results show that the MRL mouse has retained a number of molecular, metabolic, and cellular features of early embryonic and fetal cell growth. This retained, fetal-like and less well-differentiated developmental state of the MRL mouse is regulated by tightly coordinated mitochondrial metabolism.

MATERIALS AND METHODS

Animals, Injury Models, and Cell Culture

MRL/MpJ (MRL) mice were obtained from the Jackson Laboratory (Bar Harbor, ME) and C57BL/6 (B6) mice were obtained either from the Jackson Laboratory or Taconic Laboratories (Germantown, NY) and maintained on ad libitum Harlan 8604 or Labdiet Pico-Vac 20 mouse chow and water, and housed at 20°–22°C with a 12h light and dark cycle. The MRL mouse was derived from a series of crosses between LG/J (75%), C3H/HeDi (12.1%), AKR/J (12.6%), and B6 (0.3%) strains [16]. Ear punches were carried out as previously described [1] and read weekly. Primary ear skin fibroblasts and blastema-derived cells were established from MRL and B6 animals and grown in high glucose (4.5 g/L) DMEM-10% FBS supplemented with 2 mM L-glutamine, 100 IU/ml penicillin-streptomycin and maintained at 37°C, 5% CO₂, and 21% O₂, except when noted. Cells were split 1:5 as needed to maintain exponential growth and avoid contact inhibition. Passage numbers were documented and cells from early passages (<P20) frozen in liquid nitrogen and used in the described experiments. Myocardial injuries were carried out as previously described [2]. Cryoinjury to the heart was produced using a probe, cooled in liquid nitrogen, and then applied trans-diaphragmatically, causing injury to the right ventricle of the heart.

Antibodies, Microscopy, and Westerns

Primary ear-skin fibroblasts were grown on glass coverslips in Dulbecco's Modified Essential Medium DMEM with 10% fetal bovine serum at 37°C in a humidified 5% CO₂ incubator. Cells were labeled with Mitotracker Orange CMTMRos (Molecular probe Cat# M-7510). When cells reached the desired (70%) confluence, medium was removed from the dish and the prewarmed probe was added at a concentration of 100nM and incubated for 45 min at 37°C. Cells were then washed at 37°C with Hank's balanced salt solution (HBSS), fixed 15 minutes at 37°C in freshly prepared 3.7% paraformaldehyde in HBSS and coverslipped. For detection of microtubules, primary antibody monoclonal anti- α -tubulin (Sigma Cat#T9026) was used at a concentration 1:500 with secondary antibody FITC goat anti-mouse (Santa Cruz, Cat#sc-2078) at a concentration of 1:300. MABs to two mitochondrial DNA-encoded subunits of the respiratory chain (CI/ND6 20 kDa, and CIV/COXI running at an apparent 35 kDa), and three nuclear DNA-encoded subunits (CII/1p 30 kDa, CIII/Core2 47 kDa, and CV/F1a 55kDa) were obtained as a panel of antibodies for ophos immunoblots from Mitosciences (Cat# MS604, Eugene, OR) and used according to manufacturer instructions. Fibroblast samples were denatured at 95°C for 5 minutes prior to loading which resulted in elimination of the heat-sensitive COXI band. Samples (60 μ g/well) were loaded on a 10% SDS-PAGE gel. Isolated mitochondrial samples were denatured at 50°C prior to loading to permit visualization of the COXI band. These samples were run in 10 μ l at a protein concentration of 1mg/ml (10 μ g) and were loaded on a discontinuous 8–15% SDS-PAGE gel. After protein was transferred to Immobilon-P (Millipore), blots were incubated for blocking with 5% NFDM (nonfat dry milk/TBST) for 4 hrs, incubated with a 1:1000 dilution of the OXPHOS antibodies at 4°C overnight, washed with TBST, then followed by a 1: 30,000 dilution of HRP-coupled goat anti-mouse antibody. Finally, a chemiluminescent HRP substrate (Millipore; Billerica, MA, USA; cat. #WBKLS0100) was used for development of bands using HyBlot CL autoradiography film.

Immunohistochemistry

The paraffin sections were dewaxed in xylene and rehydrated. The antigen retrieval was performed by autoclaving for 20 min in 10mM Sodium Citrate, pH 6.0. The tissue sections were then treated with 3% H₂O₂ and non-specific binding was blocked with 5% Normal Rabbit Serum (for Anti-Islet-1) and 4% BSA (for Anti-Sox2 and Anti-Nanog). The primary antibodies were as follows: goat polyclonal Anti-Islet-1 (sc23590; Santa Cruz, 1:50), rabbit polyclonal Anti-Nanog (sc1000; Calbiochem, 1:100) and rabbit polyclonal Anti-Sox2 (AB5603; Chemicon, 1:1000) were incubated at 4°C overnight. The sections were reacted with secondary antibodies: the anti-Islet-1 was detected by Biotin-SP-AffiniPure F(ab¹)₂ fragment rabbit anti-goat IgG (H+L) (305-066-003; Jackson ImmunoResearch, 1:2000), the anti Nanog was detected by Alexa Fluor 568-conjugated goat anti-rabbit IgG antibody (A11036; Molecular Probe, 1:800) and anti-Sox2 was detected by biotinylated monoclonal Anti-Rabbit IgG (B5283; Sigma, 1:1000), incubated at RT for 1 hr. After washes with PBS, the sections were reacted with the reagents of the Vectastain ABC Kit (PK-6100; Vector) at RT for 1 hr. After subsequent washes, the sections were stained with DAB (SK-4100; Vector).

Histology

Tissues for frozen sections were snap frozen in liquid nitrogen and 10 μ m cryostat sections were mounted on slides for Oil Red O and PAS staining. Tissues for paraffin-embedding were fixed in the glyoxal-based dialdehyde fixative Prefer (Annatech Ltd, Battle Creek, MI) for 1 hour, then dehydrated, cleared, embedded in paraffin, and 6 μ m microtome sections mounted on slides for PAS staining.

Electron Microscopy and Morphometry

Tissues were divided into 1mm cubes by sharp dissection and fixed in Karnovsky's fixative (4% paraformaldehyde, 2.5% glutaraldehyde, 5mM CaCl₂ in 0.1M Na-cacodylate buffer, pH 7.4) for 2hrs at 4°C, then placed in 0.1M Na-cacodylate buffer, pH 7.4 until further processing. The samples were then treated with 1% OsO₄ in 0.1M Na-cacodylate buffer, pH 7.4 for 1 hr, transferred to 30% ethanol for 10min, then stained en bloc with 4% uranyl acetate in 50% ethanol, then dehydrated using a graded series of 70%–100% ethanol solutions. This was followed by propylene oxide and infiltration with epoxy resin (Scipoxy 812, Energy Beam Sciences, Agawam, MA). After polymerization at 65° C overnight, thin sections (20–50 nm) were cut and stained with uranyl acetate (4% uranyl acetate in 50% ethanol) followed by bismuth subnitrate. Sections were examined at an accelerating voltage of 60kV using a Zeiss EM10C electron microscope with images captured at 6300–16,000x to photographic negatives and printed as 8×10 glossy images to produce final magnifications of 17,325–44,000x. Mitochondria and lipid droplets in at least 3 independent fields were measured directly from the hard copy images and the dimensions converted to microns. Only hepatocyte images were used for analysis. Other liver cell types such as Kupffer cells, endothelial cells, bile ductular epithelial cells and Ito cells were identified on the basis of distinctive nuclear shape and chromatin pattern, and were excluded.

Lactate Determinations

Lactate measurements in blood and cell culture media were made with the Lactate Scout portable lactate meter (Sports Research Group, Hawthorne, NY). Cultured fibroblasts were seeded at 1×10^5 cells/well in 6-well Costar plates containing 3ml/well of DMEM-10% FBS with 25 mM glucose (Invitrogen #11965) under ambient (21%) oxygen. The medium was replaced the next day. Lactate measurements were made 24 hrs later, the plates were trypsinized, cells counted, viability determined by trypan blue exclusion, and the net lactate production was expressed as a function of cell number.

Flow Cytometry, $\Delta\Psi_m$, and ROS Determinations

Relative mitochondrial transmembrane potentials were measured in intact cells with the potentiometric, cationic carbocyanine dye DiIC₁(5) and the MitoProbe assay kit according to manufacturer instructions (Molecular Probes/Invitrogen). Briefly, exponentially growing MRL and B6 fibroblasts were harvested and adjusted to 5×10^5 cells/ml in DMEM-10% FBS with 20 mM HEPES added to maintain pH at 7.4, and 10 nM DiIC₁(5) was added from a 1 μ M stock in DMSO. The cells were incubated at 37°C for 30 min in the dark and the relative fluorescence was determined by flow cytometry with excitation at 633 nm and emission centered on 658 nm read in the FL4 channel of a BD FACSCalibur flow cytometer.

Mitochondrial reactive oxygen species (ROS) production was measured using dihydrorhodamine 123 (DHR123) by standard methods [17]. DHR123 is non-fluorescent, but is concentrated in mitochondria where it is oxidized to fluorescent rhodamine 123 in the presence of hydrogen peroxide (H₂O₂) or peroxynitrite (ONOO^{•-}). Briefly, exponentially growing MRL and B6 fibroblasts were harvested and adjusted to 5×10^5 cells/ml in DMEM-10% FBS with 20 mM HEPES added to maintain pH at 7.4 in room air. One-tenth volume of 100 μ M DHR123 (final = 10 μ M) was added from a freshly prepared stock in DMEM-10%. The cells were incubated at 37°C in the dark for 3 hrs, and fluorescence was measured in the FL1 channel of a BD FACSCalibur flow cytometer. The geometric mean of the autofluorescence tubes (cells incubated in the absence of DHR123) was subtracted and RH123-specific fluorescence quantified.

Cellular and Tissue Glutathione Content

Total cellular glutathione content was quantified in a colorimetric microplate assay based on DTNB formation of 2-nitro-5-thiobenzoic acid developed by Anderson [18] using the Dojindo glutathione quantification kit (T419-10, Dojindo Molecular Technologies, Gaithersburg, MD). Briefly, exponentially growing fibroblasts were harvested and washed in PBS. Cell pellets containing $0.5\text{--}1 \times 10^6$ cells were suspended in $80 \mu\text{l}$ of 10 mM HCl, mixed and lysed by 2 freeze-thaw cycles. The samples were deproteinized by addition of $20 \mu\text{l}$ of 5% sulfosalicylic acid (SSA) and centrifugation at $8000g \times 10 \text{ min}$. The deproteinized supernatants were transferred to fresh tubes for assay. For tissue glutathione determinations, liver and heart samples were collected from 12-week old MRL and B6 mouse females. Approximately 33 mg samples were taken from the frozen organs from three individuals to form 100 mg pools. The tissue pools were homogenized in 250 mM sucrose (100 mg tissue/ml) with a pyrex glass pestle homogenizer, followed by two freeze-thaw cycles. A portion of each sample was removed to a separate tube for total protein determination. Total protein was measured by solubilizing the sample in 9 volumes of lysis buffer (Tris-Cl 50 mM pH 6.8, DTT 100 mM, SDS 2%) and heating for 10 min at 95°C , then measured by Bradford assay. The remaining tissue samples were deproteinized by adding sufficient 20% sulfosalicylic acid (SSA) to obtain a 4% SSA concentration. Precipitated protein was removed by centrifugation at $[8000g \times 2 \text{ min}]$ and the supernatants were diluted to 0.8% SSA for glutathione determination. Total glutathione was determined for four dilutions of each sample in a microplate assay using Total Glutathione Quantification Kit (Dojindo Laboratories, cat. no. T419-10) according to manufacture's instructions. Absorbance was measured on a BioRad Plate Reader Model 550 at 405 nm.

Mitochondrial DNA Quantitation

Total cellular DNA was isolated from heart, skeletal muscle, and liver from 10 week old MRL or C57BL/6 females using the Puregene DNA isolation kit (Gentra Systems, MN). Quantitative real-time PCR was performed using an ABI-7300 Real-Time PCR system and the ratio of multicopy mouse mitochondrial DNA (mtDNA) to single-copy nuclear DNA (nDNA) was determined according to the method of Moreno-Loshuertos, et al [19]. Primers directed toward subunit II of the mitochondrial cytochrome c oxidase gene (mCOXII-F-5'—CTACAAGACGCCACAT; mCOXII-R-5'—GAGAGGGGAGAGCAAT) were used to amplify a 216 bp fragment of mouse mtDNA. Primers directed toward the single-copy nuclear gene, succinate dehydrogenase subunit A (mSDHA-F-5'—TACTACAGCCCCAAGTCT; mSDHA-R-5'—TGGACCCATCTTCTATGC) were used to amplify a 193 bp fragment of nuclear DNA. Reactions were performed in $25 \mu\text{l}$ using the Platinum SYBR Green qPCR Supermix-UDG with ROX from Invitrogen. Primer and MgCl_2 concentrations were $0.2 \mu\text{M}$ and 3 mM , respectively. Four-point dilution curves were performed with 1–20 ng of total input DNA to verify uniform amplification efficiencies of DNA from each tissue. The PCR program was: 50° for 2 min \times 1 cycle for UDG; 95° for 10 min \times 1; then [95° for 15 sec, and 60° for 1 min] \times 40 cycles. The ratio of mtDNA to nDNA was determined by ΔC_T analysis. Melting curves were performed with each run and confirmed the absence of primer dimers and uniform T_m s for each gene amplified from different tissues.

Nanog RT-QPCR

Total RNA was isolated from ventricular myocardium before and 1-week after cryoinjury, and 100ng was reverse transcribed using SuperScript III First Strand Synthesis SuperMix for qRT-PCR (Cat# 11752-050, Invitrogen) according to instructions. The resulting cDNA was diluted 3-fold in RNase and DNase-Free (RDF) water, then analyzed by real-time QPCR in an ABI-7300 Real-Time PCR system. Mouse β -actin (m β -ActinF-5'—TTCCTTCTTGGGTATGGAAT, m β -ActinR-5'—GAGCAATGATCTTGATCTTC) and

Nanog (mNanog-F-5'-AGGGTCTGCTACTGAGATGCTCTG, mNANOG-R-5'-CAACCACTGGTTTTTCTGCCACCG) QPCR primers [20] were used at a final concentration of 0.3 μ M. Serial 2-fold dilutions of cDNA were used to verify equal amplification efficiencies. QPCR was conducted in 25 μ l reactions using Platinum SYBR Green qPCR Supermix-UDG with ROX (Cat# 11744-100, Invitrogen). The PCR program was: 50° for 2 min \times 1 cycle for UDG; 95° for 10 min \times 1; then [95° for 15 sec, and 60° for 1 min] \times 40 cycles, followed by melting curve analysis to exclude primer-dimer formation and product uniformity. The abundance of NANOG mRNA was expressed as a ratio to β -actin by ΔC_t analysis.

Mitochondrial Isolation

Liver mitochondria for respiratory chain enzymology were isolated by the method of Rossignol, et al [21] then frozen at 5–10 mg/ml in liquid nitrogen for further study. Heart mitochondria for enzymology and polarography were isolated as described by Taylor and Turnbull after removal of the atria [22], and resuspended at a concentration of 20–50 mg/ml in 0.25M sucrose, 0.1mM K-EGTA, 2mM HEPES pH 7.4. Liver mitochondria for polarography were isolated by a modification of Hoppel, *et al.* [23] and analyzed on the same day of preparation, without freezing. Briefly, livers were isolated from 16-week old females fed ad libitum and sacrificed by cervical dislocation. The gall bladder was removed and the liver collected directly into 10 ml of ice-cold MSM buffer (220mM mannitol, 70mM sucrose, 5mM MOPS pH 7.4, 2mM K-EGTA). All further processing was performed at 4°C on crushed ice. The liver was rinsed in 10 ml ice cold MSM, weighed, minced into 1mm cubes, rinsed again with fresh MSM and then decanted. The washed and minced liver cubes were homogenized in 9 volumes of ice-cold MSM with 2 strokes of a chilled, loose-fitting, Potter-Elvehjem teflon-glass homogenizer driven by a slow rpm electric drill. Unbroken cells, nuclei and membrane-associated debris were removed by centrifugation at 400g \times 10 min at 4°C in an SS-34 rotor. The supernatant was collected and filtered through gauze to remove excess lipid, then centrifuged 7000g \times 10 min at 4°C. The mitochondria-rich pellet was resuspended in 10 ml ice-cold MSM per gram liver wet weight, then washed two more times by centrifugation at 7000g \times 10 min at 4°C. The washed mitochondrial pellet was then resuspended in 0.2 ml MSM per gram of liver wet weight to yield a mitochondrial protein concentration of about 50–100 mg/ml determined by Lowry assay.

Respiratory Chain Enzymology

The enzymatic activity of mitochondrial complex I was measured as NADH:CoQ1 oxidoreductase activity by the method of Taylor and Turnbull [22]. Complex II was measured as succinate:CoQ1 oxidoreductase activity by the method of Birch-Machin and Turnbull [24]. Complex II/III was measured as succinate:cytochrome c reductase activity by the method of Stumpf and Parks [25]. Complex IV was measured as cytochrome c oxidase activity by the method of Taylor and Turnbull [22] and expressed as an apparent first order rate constant. Citrate synthase activity was used as a marker of mitochondrial mass and was measured by the method of Shepherd and Garland [26]. Rates were expressed as the ratio of respiratory chain enzyme activity to citrate synthase activity.

Mitochondrial Polarography

High resolution polarography was performed using an Oroboros Oxygraph 2k respirometer under DatLab 4.2.0.73 software control (Innsbruck, Austria). Four hundred-800 μ g of freshly isolated liver mitochondria from 16 week-old age matched females were introduced into 2ml polarographic chambers containing MiR05 [27] (110mM sucrose, 60mM K-lactobionate, 20mM taurine, 20mM HEPES pH 7.1 with KOH, 10mM KH₂PO₄, 3mM MgCl₂, 0.5mM EGTA, 1mg/ml fatty acid-free BSA) respiration medium and assayed at 37°C. The following additions were made and the resulting oxygen consumption rates were

measured in units of pmol/sec/mg mitochondrial protein: 1) 2mM malate, 2) 5mM pyruvate, 3) 2mM ADP, 4) 10mM glutamate, 5) 1mM octanoyl-carnitine, 6) 10 mM succinate, 7) 10 μ g/ml oligomycin, 8) 1 μ M FCCP, 9) 12.5 μ M antimycin A. Substrate-specific respiration was measured after each addition under conditions of saturating (1–2mM) ADP.

Statistics

Values were expressed as the mean \pm SD. Differences between paired groups were assessed by Student's t-test.

RESULTS

Mitochondrial Morphology and Cytoskeletal Associations

Mitochondrial structure and organization is strongly correlated with the bioenergetic [28] and differentiation state [29] of the cell. We examined the association of mitochondria with the α -tubulin cytoskeleton in both B6 and MRL ear skin fibroblasts (Fig. 1ABC and 1DEF). In fibroblasts from the non-healer B6 mice, mitochondria were patchy in their distribution, and were elaborated into a reticular network within the cell (indicated by the arrows in Fig. 1B). In contrast, the mitochondria of the healer MRL mice, were radially distributed from the nucleus, without any evidence of significant reticulum formation or major axis (Fig. 1E).

Metabolic Features of MRL Cells and Mitochondria

Mitochondrial Transmembrane Potential—The bioenergetic capacity of a mitochondrion is determined by its transmembrane potential ($\Delta\Psi_m$), which can be assessed by uptake of fluorescent, mitochondriotropic, potentiometric probes such as DiIC₁(5). We found that the $\Delta\Psi_m$ of healer MRL fibroblast mitochondria was significantly less polarized (less electronegative) than B6 cell mitochondria (Fig. 1g, green and red tracings, respectively). Further, we found that when blastema-derived cells were isolated from the 17-day healing ear hole margins of MRL mice, the mitochondrial transmembrane potential was further reduced (Fig. 1g, orange tracing). The reduced mitochondrial transmembrane potential does not imply the cells are less “energetic”. Instead, it indicates a shift in cellular bioenergetics away from oxygen-dependent ATP synthesis by oxidative phosphorylation in mitochondria, to non-oxygen-requiring ATP synthesis in the cytosol by glycolysis.

Lactate Production—Lactate production is a measure of the cellular bioenergetic dependence on glycolysis. If less ATP is made by oxidative phosphorylation in mitochondria, the rate of glycolysis is increased to meet cellular demands. We found that the lactate production of MRL ear skin fibroblasts was more than double the production in B6 cells (51.8 \pm 4.5 vs 23.4 \pm 0.9 pmol/cell/day, Fig. 1h), indicating an increased rate of glycolysis in MRL cells.

Reactive Oxygen Species—Reactive oxygen species (ROS) homeostasis plays a critical role in cell signaling, growth and differentiation [30]. Multipotential stem cells have a low-ROS phenotype [31], while many cancer cells have a high-ROS phenotype [32]. Both embryonic stem (ES) cells and cancer cells are dedifferentiated, but ES cells retain genomic stability and the capacity for terminal differentiation, while most cancer cells with a high-ROS phenotype exhibit genomic instability and sharply limited capacity for terminal differentiation. We measured the ROS phenotype in primary MRL fibroblasts compared to non-healer control cells from B6. We found that MRL fibroblast mitochondria produced significantly less ROS, resulting in a 4-fold reduction in ROS-associated fluorescence (B6 41.5 \pm 4.2; MRL 11.6 \pm 0.61; Fig. 1i).

Glutathione—Intracellular glutathione was measured as an index of the magnitude of cellular resources devoted to antioxidant defense. Consistent with the reduced ROS production found in MRL skin fibroblasts, MRL primary fibroblasts and liver showed a 42% and 35% reduction in total glutathione pools, respectively, compared to B6 (Fig. 1j and l). There was no difference found in the heart (Fig. 1k).

Molecular and Functional Features of MRL Cells and Mitochondria

Tissue Mitochondrial Content—Citrate synthase (CS) is a Krebs cycle enzyme that is a specific marker of the mitochondrial matrix [26]. CS activity per gram of tissue is a measure of the total mitochondrial matrix content of the tissue, while CS activity per mg of mitochondrial protein is a measure of the CS concentration in the mitochondrial matrix. We found that the MRL liver contained 67% more mitochondrial CS than B6 (Fig. 2A; MRL 9.0+/-1.4 vs B6 5.4+/-1.4 CS Units/g liver). The packing density of MRL and B6 mitochondria was similar (Fig. 2B; MRL 0.417+/-0.038 vs B6 0.396+/-0.059 U/mg mitochondria), but the total mitochondrial mass was over 50% higher in the MRL liver (Fig. 2C; MRL 21.7+/-2.8 vs B6 14.2+/-2.9 mg/g liver). Therefore, the increased CS in the MRL liver was due to an increase in mitochondrial content. The situation was different in the heart. The MRL heart contained 82% more mitochondrial CS than B6 (Fig. 2E; MRL 21.1+/-0.94 vs 11.6+/-0.69 U/g heart). In contrast to liver mitochondria, the packing density of MRL heart mitochondria was 62% higher than B6 (Fig. 2F; MRL 4.58+/-0.16 vs B6 2.82+/-0.11 U/mg mitochondria) and the total mitochondrial mass was 12% higher (Fig. 2G; MRL 4.62+/-0.21 vs B6 4.10+/-0.25 mg/g heart). These results show that that the increased CS in the MRL heart (Fig. 2E) was due predominantly to an increase in mitochondrial packing density (Fig. 2F), while only about 15% was due to an increase in total mitochondrial mass in MRL hearts (Fig. 2G). In both liver and heart, the overall mitochondrial protein content was significantly greater in the MRL mouse than that of the non-healer B6 (Fig. 2C and 2G).

Mitochondrial DNA Content—The mitochondrial DNA content of non-healer B6 and healer MRL tissues was measured by real-time quantitative PCR (QPCR). We found that the MRL liver contained 60% more mtDNA than B6 (106 vs 66 mtDNA/nDNA Fig. 2D). The heart had over 4-fold more mtDNA in MRL than the non-healer B6 (184 vs. 43; Fig. 2H).

Stem Cell Marker Expression

Nanog is a transcription factor thought to be important in multipotency and is expressed in embryonic stem cells. If the MRL mouse shows fetal-like characteristics like aerobic glycolysis, along with a regenerative potential, could it express such a marker? We examined the expression of Nanog mRNA as a marker of differentiation potential in the hearts of healer and non-healer mice at baseline and 7-days after cryoinjury. Interestingly, the hearts of adult MRL mice, but not B6 mice, exhibited detectable Nanog expression at baseline (Fig. 3a; B6= Undetectable; MRL= 56 +/-9, units expressed relative to β -actin mRNA $\times 10^6$). One week after right ventricular cryoinjury, Nanog mRNA was induced almost 10-fold in MRL mice, and was also induced in the B6, but only to just 2% of the expression level observed in the MRL (Fig. 3a; B6 = 8.3 +/-3; MRL= 426 +/-14). Expression of Nanog was investigated at the protein level in the heart using immunohistochemistry, before and after cryoinjury (Fig. 3b). Nanog was not detectable in control B6 animals before injury and was present only in a few cells near the epicardium after injury (Fig. 3bAB). In contrast, Nanog was present in a monolayer of cells at the epicardium before injury (Fig. 3bC). After injury in the MRL mouse, Nanog was found in several cell layers in the epicardium, with a gradient of cells that appeared to be migrating into, or activated in, deeper layers of the myocardium (Figs. 3bD).

Since Nanog was expressed in adult MRL heart, we looked for the expression of other markers of pluripotential, stem cell-like proliferative potential. We found that Islet-1 was absent in B6 hearts before injury (Fig. 3bE), and was present in a few cells of the epicardium after injury at the injury site (Fig. 3bF). Islet-1 was strongly positive in cells of the epicardium (Fig. 3bG) and endocardium (not shown) in the adult MRL heart before injury, and was found in several cell layers of the epicardium after injury (Fig. 3bH). Likewise, Sox2 was absent in B6 epicardium (not shown) and endocardium before injury (Fig. 3bI) and was present in a few cells of the epicardium after injury (Fig. 3bJ). In contrast, Sox2 was abundantly present in cells of the endocardium before injury in the MRL (Fig. 3bK), and was observed in many cells of the epicardium and heart after injury (Fig. 3bL).

Respiratory Chain Protein Composition

We next turned to Western analysis of critical subunits of the mitochondrial electron transport chain to gather subunit-specific information about the proteins of mitochondrial oxidative phosphorylation, and their stoichiometry. The proteins selected for interrogation represent core proteins that are essential for the assembly of each of the 5 major complexes of the mitochondrial respiratory chain. MRL primary ear skin fibroblasts showed a reduction in the 47 kD core 2 subunit of complex III compared to B6 (Fig. 4a). MRL blastema-derived primary ear skin fibroblasts showed the restoration of this subunit, and a dramatic increase in the expression of the F1a subunit of complex V, the ATP synthase, and Complex I (Fig. 4a). In isolated mitochondria from liver and heart we found an increase in Complex I expression (Fig. 4b).

We next examined the kinetics of mitochondrial respiratory chain protein expression in response to ear hole injury. Before injury, MRL ear pinnae homogenates showed a decreased expression of the mtDNA-encoded, 20 kD subunit of Complex I gene for ND6 (Fig. 4c, Day 0). One day after injury, both MRL and B6 rapidly reduced the expression of both nucleus-encoded and mtDNA-encoded subunits of the mitochondrial electron transport chain (Fig. 4c, Day 1). On day 10 after injury, both B6 and MRL mice showed recovery of expression of the nucleus-encoded subunits of complexes II, III, and V. However, MRL maintained strongly reduced expression of the mtDNA-encoded, 20 kD complex I protein through day 10 (Fig. 4c, Day 10).

Respiratory Chain Biochemistry and Oxidative Phosphorylation

A consistent pattern emerged when the functional status of the mitochondrial respiratory chain complexes was measured enzymatically. In both heart and liver mitochondria of the healer MRL mice, at least 2 of the 4 electron transport chain complexes were reduced under baseline conditions, compared to the non-healer B6 respiratory chain. In the liver the more distal complexes III and IV were decreased, while in heart, the more proximal complexes I and II were decreased (Fig. 5). The reduced activity of the respiratory chain in the healer MRL mice was consistent with the increased lactate production and decreased mitochondrial transmembrane potential ($\Delta\Psi_m$).

High resolution polarography was used to assess the functional oxidative phosphorylation (oxphos) capacity of isolated B6 and MRL liver mitochondria. We found that MRL mitochondria had a 27% reduction in fatty acid (octanoyl carnitine) oxidation compared to B6. MRL also showed a 21% increase in glutamate oxidation (Fig. 6ab). The maximum uncoupled respiratory capacity of mitochondria from MRL and B6 mice was equivalent. These findings show that although the uncoupled respiratory chain capacity was the same in B6 and MRL mice, there were significant differences in the way that specific metabolic substrates are handled.

Alterations in Glycogen and Lipid Storage

Oil red O staining of neutral lipid in the B6 liver showed a generally uniform distribution and reduced concentration of oil red O staining (Fig. 6c-AC). The MRL liver had more lipid overall (Fig. 6c-BD) than B6, consistent with the observed reduction in fatty acid oxidation. In addition, the lipid droplets in the MRL showed a patchy distribution, indicating the presence of metabolic mosaicism for fatty acid oxidation and synthesis between hepatocytes in the MRL liver (Fig. 6c-BD). No differences were observed under polarizing microscopy, which was used to test for birefringent cholesterol esters versus the non-birefringent glycerol esters of lipid (data not shown). PAS staining was used to examine the glycogen content in the B6 and MRL liver. The B6 liver showed a patchy distribution of high-, and low-glycogen-containing hepatocytes (Fig. 6c-E). In contrast, PAS staining of the MRL liver showed a uniform distribution of hepatocellular glycogen that appeared tightly distributed around the hepatocellular nuclei (Fig. 6c-F). Electron microscopy revealed the presence of lipid droplets and more spherically shaped mitochondria in the MRL liver (Fig. 6c-H). Lipid droplets were not observed in the B6 liver (Fig. 6c-G). The reduced glycogen content in the MRL liver is consistent with increased glycolysis. The increased lipid content is consistent with the observed decrease in mitochondrial fatty acid oxidation.

DISCUSSION

Mitochondria are essential for the life and death of eukaryotic cells [33] and are increasingly being recognized as playing key roles in the pathogenesis in a number of diseases in both children [34,35] and adults [36]. We were struck by the similarities between the dynamic coordination of mitochondrial metabolism in normal embryonic development [37,38], and the cellular changes that accompany the extraordinary healing phenotype of the MRL mouse [39]. We set out to explore the basis for these similarities in this report.

Animal cell mitochondria maintain important cytoskeletal associations with intermediate filaments [40] and microtubules [29]. These associations participate in normal fusion-fission dynamics [41], and the resulting changes in morphology and subcellular distribution of mitochondria have recently been shown to be tightly correlated with growth and differentiation in a number of cell types, including stem cells [42]. As in stem cells, the mitochondria in MRL fibroblasts are concentrated around the nucleus and tightly associated with microtubules in linear arrays (Fig. 1DEF). In contrast, the mitochondria of B6 fibroblasts extended in a reticular network from the nucleus to the cell membrane, and exhibited clusters of organelles (Fig. 1ABC) that were similar to the pattern observed in stem cell cultures that had undergone partial differentiation and had lost pluripotentiality [42].

The emphasis on glycolytic energy metabolism with increased lactate production in MRL cells (Fig. 1h), while maintaining normal oxygen consumption is reminiscent of the Warburg effect of aerobic glycolysis in cancer [43], normal development [44], and in normal wound healing [45]. However, in contrast to most cancer cells from solid tissues, which have hyperpolarized mitochondrial transmembrane potentials ($\Delta\Psi_m$) [46] and increased reactive oxygen species (ROS) production [32], MRL fibroblasts had a reduced $\Delta\Psi_m$ (Fig. 1g) and reduced ROS production (Fig. 1i). Mitochondrial ROS are produced by the incomplete reduction of ubiquinone (CoQ10) to its semiquinone form, with single electron transfer from semiquinone to molecular oxygen to make superoxide ($O_2^{\cdot-}$). This occurs principally at respiratory chain complexes I and III [47]. Primary reductions in mitochondrial transmembrane potential create a situation in which less electrochemical energy is available for reactive oxygen production in mitochondria [48]. Thus, the two findings of reduced $\Delta\Psi_m$ and reduced ROS in MRL cells may be causally related. This situation is similar to pluripotential stem cells, primary oocytes, pluripotential cells of the

blastocyst inner cell mass (ICM) [49], and hematopoietic stem cells [31] which also have a reduced mitochondrial transmembrane potential and reduced ROS. Also unlike many cancer cells which exhibit mtDNA depletion [50], we found that the mtDNA content was increased (Fig. 2dh), and total mitochondrial protein was increased (Fig. 2), yet the activity of the mitochondrial electron transport chain was reduced under baseline conditions (Fig. 5). These findings revealed a large genetic and metabolic reserve in MRL cell mitochondria, defined as an underutilized increase in mtDNA and respiratory chain protein content. Interestingly, a similar increase in mitochondrial functional reserve capacity has recently been shown to be a major determining factor in neuronal cell survival in response to toxin exposure and glutamate toxicity [51].

At the level of gene expression, we found that adult MRL mice retained detectable expression of several stem cell markers including Nanog (Fig. 3bCD), Islet-1 (Fig. 3bGH), and Sox2 (Fig. 3bKL). After a heart cryoinjury, Nanog was induced in MRL nearly 10-fold, and this level of expression was over 50-fold higher than in the non-healer B6 strain. Nanog is well-known as an essential molecule for maintenance of pluripotential stem cells [52,53]. Retention of these stem cell markers is strong evidence of the existence of relatively undifferentiated cells even in highly differentiated tissue of the adult MRL mouse. While retention of fetal-like features of metabolism in adulthood is rare in mammals, the axolotl, a classical fully regenerating species, does maintain an immature phenotype as an adult [54]. Our results in the MRL mouse provide a strong incentive for re-examination of the metabolic underpinning of regeneration in classical regenerating species like the axolotl, newt, and *Planaria*. These studies have implications for adult mammalian cell manipulations with small molecule drugs designed to stimulate metabolic networks associated with healing in the embryo, and regeneration in other species.

In the MRL liver, we found that fatty acid oxidation was reduced and glutamate oxidation was increased (Fig. 6ab). Glutamate has several fates in the liver. It can be used anabolically in the cytosol to provide carbon skeletons for citrate and lipid synthesis. In this pathway, glutamate is converted to α -ketoglutarate by transamination with alanine by aspartate transaminase. Then under reducing conditions, the cytosolic α -ketoglutarate is converted sequentially to isocitrate by cytosolic isocitrate dehydrogenase, and to citrate by cytosolic aconitase. The resulting citrate can be used for fatty acid synthesis [55]. In the MRL liver however, glutamate is converted to α -ketoglutarate and shunted preferentially to mitochondria for oxidation. The entry of carbon skeletons into the Krebs cycle to increase the availability of Krebs cycle intermediates is called anaplerosis. When glutamate is used anaplerotically, it is shunted away from the cytosol. The anaplerotic use of glutamate [56], combined with export of malate and citrate from mitochondria, are central features of the Warburg effect observed in cancer cells and in embryonic metabolism [57,58]. The export of malate from mitochondria results in the synthesis of reducing equivalents of NADPH for glutathione recycling and macromolecule synthesis through the action of malic enzyme and the conversion of malate to pyruvate in the cytoplasm.

Several studies have shown a correlation between reduced fatty acid oxidation and enhanced recovery from injury [59]. The cardioprotective effect of the naturally reduced fatty acid oxidation capacity of MRL mice may help to explain the observed enhancement in recovery from heart injury [2]. The combination of decreased fatty acid oxidation and increased aerobic glycolysis has the net effect of favoring the accumulation of intrahepatic stores of lipid. This was confirmed histologically by oil red O staining for neutral lipid in the MRL liver (Fig. 6c). Our results demonstrate that retention of embryonic metabolic traits of mitochondrial reserve capacity, aerobic glycolysis, and stem cell marker expression in adult MRL mice sharply distinguishes them from control non-regenerating C57BL/6 mice.

Acknowledgments

This work was supported in part by grants to EH-K from the F.M. Kirby Foundation, the W.W. Smith Charitable Trust, the G. Harold and Leila Y. Mathers Charitable Foundation, from the Commonwealth of Pennsylvania and the PA Breast Cancer Coalition, and an NCI Cancer Center Grant (P30 CA10815) to the Wistar Institute. RKN was supported by gifts from the UCSD Foundation Christini Fund, the Lennox Foundation, the Engs Family Living Trust, and many families who have contributed support for mitochondrial disease research at the MMDC. The authors thank Susanna Petrosyan for expert technical assistance.

References

1. Clark LD, Clark RK, Heber-Katz E. A new murine model for mammalian wound repair and regeneration. *Clin Immunol Immunopathol.* 1998; 88:35–45. [PubMed: 9683548]
2. Leferovich JM, Bedelbaeva K, Samulewicz S, Zhang XM, Zwas D, Lankford EB, Heber-Katz E. Heart regeneration in adult MRL mice. *Proc Natl Acad Sci U S A.* 2001; 98:9830–9835. [PubMed: 11493713]
3. Stocum, DL. *Regenerative Biology and Medicine.* Academic; New York, NY: 2006.
4. Brockes JP, Kumar A. Appendage regeneration in adult vertebrates and implications for regenerative medicine. *Science.* 2005; 310:1919–1923. [PubMed: 16373567]
5. Edwards RG. From embryonic stem cells to blastema and MRL mice. *Reprod Biomed Online.* 2008; 16:425–461. [PubMed: 18339268]
6. Samulewicz SJ, Seitz A, Clark L, Heber-Katz E. Expression of preadipocyte factor-1(Pref-1), a delta-like protein, in healing mouse ears. *Wound Repair Regen.* 2002; 10:215–221. [PubMed: 12191003]
7. Srivastava AK, Mohan S, Masinde GL, Yu H, Baylink DJ. Identification of quantitative trait loci that regulate obesity and serum lipid levels in MRL/MpJ x SJL/J inbred mice. *J Lipid Res.* 2006; 47:123–133. [PubMed: 16254318]
8. Heber-Katz E, Chen P, Clark L, Zhang XM, Troutman S, Blankenhorn EP. Regeneration in MRL mice: further genetic loci controlling the ear hole closure trait using MRL and M.m. Castaneus mice. *Wound Repair Regen.* 2004; 12:384–392. [PubMed: 15225218]
9. Ichii O, Konno A, Sasaki N, Endoh D, Hashimoto Y, Kon Y. Autoimmune glomerulonephritis induced in congenic mouse strain carrying telomeric region of chromosome 1 derived from MRL/MpJ. *Histol Histopathol.* 2008; 23:411–422. [PubMed: 18228198]
10. Miyazaki T, Ono M, Qu WM, Zhang MC, Mori S, Nakatsuru S, Nakamura Y, Sawasaki T, Endo Y, Nose M. Implication of allelic polymorphism of osteopontin in the development of lupus nephritis in MRL/lpr mice. *Eur J Immunol.* 2005; 35:1510–1520. [PubMed: 15832294]
11. Zheng QY, Johnson KR, Erway LC. Assessment of hearing in 80 inbred strains of mice by ABR threshold analyses. *Hear Res.* 1999; 130:94–107. [PubMed: 10320101]
12. Zhou X, Jen PH, Seburn KL, Frankel WN, Zheng QY. Auditory brainstem responses in 10 inbred strains of mice. *Brain Res.* 2006; 1091:16–26. [PubMed: 16516865]
13. Johnson KR, Zheng QY, Bykhovskaya Y, Spirina O, Fischel-Ghodsian N. A nuclear-mitochondrial DNA interaction affecting hearing impairment in mice. *Nat Genet.* 2001; 27:191–194. [PubMed: 11175788]
14. Sachadyn P, Zhang XM, Clark LD, Naviaux RK, Heber-Katz E. Naturally occurring mitochondrial DNA heteroplasmy in the MRL mouse. *Mitochondrion.* 2008
15. Maniatakis E, Mourelatos Z. Human mitochondrial tRNAMet is exported to the cytoplasm and associates with the Argonaute 2 protein. *RNA.* 2005; 11:849–852. [PubMed: 15872185]
16. Murphy, ED.; Roths, JB. Autoimmunity and lymphoproliferation: induction by mutant lpr and acceleration by a male-associated factor in strain BXSB. In: Rose, NR.; Bigazzi, PE.; Warner, NL., editors. *Genetic Control of Autoimmune Disease.* Elsevier; New York: 1979. p. 207-220.
17. Rinaldi M, Moroni P, Paape MJ, Bannerman DD. Evaluation of assays for the measurement of bovine neutrophil reactive oxygen species. *Vet Immunol Immunopathol.* 2007; 115:107–125. [PubMed: 17067684]
18. Anderson ME. Determination of glutathione and glutathione disulfide in biological samples. *Methods Enzymol.* 1985; 113:548–555. [PubMed: 4088074]

19. Moreno-Loshuertos R, Acin-Perez R, Fernandez-Silva P, Movilla N, Perez-Martos A, Rodriguez de Cordoba S, Gallardo ME, Enriquez JA. Differences in reactive oxygen species production explain the phenotypes associated with common mouse mitochondrial DNA variants. *Nat Genet.* 2006; 38:1261–1268. [PubMed: 17013393]
20. Rodic N, Oka M, Hamazaki T, Murawski MR, Jorgensen M, Maatouk DM, Resnick JL, Li E, Terada N. DNA methylation is required for silencing of ant4, an adenine nucleotide translocase selectively expressed in mouse embryonic stem cells and germ cells. *Stem Cells.* 2005; 23:1314–1323. [PubMed: 16051982]
21. Rossignol R, Letellier T, Malgat M, Rocher C, Mazat JP. Tissue variation in the control of oxidative phosphorylation: implication for mitochondrial diseases. *Biochem J.* 2000; 347(Pt 1):45–53. [PubMed: 10727400]
22. Taylor, RW.; Turnbull, DM. Laboratory diagnosis of mitochondrial disease. In: Applegarth, DA.; Dimmick, JE.; Hall, JG., editors. *Organelle Diseases: Clinical Features, Diagnosis, Pathogenesis, and Management.* Chapman & Hall Medical; London, UK: 1997. p. 341-350.
23. Hoppel CL, Kerner J, Turkaly P, Turkaly J, Tandler B. The malonyl-CoA-sensitive form of carnitine palmitoyltransferase is not localized exclusively in the outer membrane of rat liver mitochondria. *J Biol Chem.* 1998; 273:23495–23503. [PubMed: 9722587]
24. Birch-Machin MA, Turnbull DM. Assaying mitochondrial respiratory complex activity in mitochondria isolated from human cells and tissues. *Methods Cell Biol.* 2001; 65:97–117. [PubMed: 11381612]
25. Stumpf DA, Parks JK. Human mitochondrial electron transport chain: assay of succinate: cytochrome c reductase in leukocytes, platelets and cultured fibroblasts. *Biochem Med.* 1981; 25:234–238. [PubMed: 6269538]
26. Shepherd D, Garland PB. Citrate synthase from rat liver. *Methods in Enzymology.* 1969; 13:11–16.
27. Gnaiger, E.; Kuznetsov, AV.; Schneeberger, S.; Seiler, R.; Brandacher, G.; Steurer, W.; Margreiter, R. Mitochondria in the cold. In: Heldmaier, G.; Klingenspor, M., editors. *Life in the Cold.* Springer; New York: 2000. p. 431-442.
28. Benard G, Bellance N, James D, Parrone P, Fernandez H, Letellier T, Rossignol R. Mitochondrial bioenergetics and structural network organization. *J Cell Sci.* 2007; 120:838–848. [PubMed: 17298981]
29. Katayama M, Zhong Z, Lai L, Sutovsky P, Prather RS, Schatten H. Mitochondrial distribution and microtubule organization in fertilized and cloned porcine embryos: implications for developmental potential. *Dev Biol.* 2006; 299:206–220. [PubMed: 16945363]
30. Valko M, Leibfritz D, Moncol J, Cronin MT, Mazur M, Telser J. Free radicals and antioxidants in normal physiological functions and human disease. *Int J Biochem Cell Biol.* 2007; 39:44–84. [PubMed: 16978905]
31. Jang YY, Sharkis SJ. A low level of reactive oxygen species selects for primitive hematopoietic stem cells that may reside in the low-oxygenic niche. *Blood.* 2007
32. Fruehauf JP, Meyskens FL Jr. Reactive oxygen species: a breath of life or death? *Clin Cancer Res.* 2007; 13:789–794. [PubMed: 17289868]
33. Kroemer G, Reed JC. Mitochondrial control of cell death. *Nat Med.* 2000; 6:513–519. [PubMed: 10802706]
34. Naviaux RK. Developing a systematic approach to the diagnosis and classification of mitochondrial disease. *Mitochondrion.* 2004; 4:351–361. [PubMed: 16120397]
35. DiMauro S, Gurgel-Giannetti J. The expanding phenotype of mitochondrial myopathy. *Curr Opin Neurol.* 2005; 18:538–542. [PubMed: 16155436]
36. Wallace DCA. Mitochondrial Paradigm of Metabolic and Degenerative Diseases, Aging, and Cancer: A Dawn for Evolutionary Medicine. *Annu Rev Genet.* 2005; 39:359–407. [PubMed: 16285865]
37. Lust WD, Pundik S, Zechel J, Zhou Y, Buczek M, Selman WR. Changing metabolic and energy profiles in fetal, neonatal, and adult rat brain. *Metab Brain Dis.* 2003; 18:195–206. [PubMed: 14567470]

38. Makinde AO, Kantor PF, Lopaschuk GD. Maturation of fatty acid and carbohydrate metabolism in the newborn heart. *Mol Cell Biochem.* 1998; 188:49–56. [PubMed: 9823010]
39. Heber-Katz E, Leferovich J, Bedelbaeva K, Gourevitch D, Clark L. The scarless heart and the MRL mouse. *Philos Trans R Soc Lond B Biol Sci.* 2004; 359:785–793. [PubMed: 15293806]
40. Collier NC, Sheetz MP, Schlesinger MJ. Concomitant changes in mitochondria and intermediate filaments during heat shock and recovery of chicken embryo fibroblasts. *J Cell Biochem.* 1993; 52:297–307. [PubMed: 8103523]
41. Frazier AE, Kiu C, Stojanovski D, Hoogenraad NJ, Ryan MT. Mitochondrial morphology and distribution in mammalian cells. *Biol Chem.* 2006; 387:1551–1558. [PubMed: 17132100]
42. Lonergan T, Brenner C, Bavister B. Differentiation-related changes in mitochondrial properties as indicators of stem cell competence. *J Cell Physiol.* 2006; 208:149–153. [PubMed: 16575916]
43. Warburg O, Posener K, Negelein E. Über den Stoffwechsel der Tumoren. *Biochemische Zeitschrift.* 1924; 152:319–344.
44. Khurana NK, Niemann H. Energy metabolism in preimplantation bovine embryos derived in vitro or in vivo. *Biol Reprod.* 2000; 62:847–856. [PubMed: 10727252]
45. Hunt TK, Aslam RS, Beckert S, Wagner S, Ghani QP, Hussain MZ, Roy S, Sen CK. Aerobically Derived Lactate Stimulates Revascularization and Tissue Repair via Redox Mechanisms. *Antioxid Redox Signal.* 2007; 9:1115–1124. [PubMed: 17567242]
46. Bonnet S, Archer SL, Allalunis-Turner J, Haromy A, Beaulieu C, Thompson R, Lee CT, Lopaschuk GD, Puttagunta L, Bonnet S, Harry G, Hashimoto K, Porter CJ, Andrade MA, Thebaud B, Michelakis ED. A mitochondria-K⁺ channel axis is suppressed in cancer and its normalization promotes apoptosis and inhibits cancer growth. *Cancer Cell.* 2007; 11:37–51. [PubMed: 17222789]
47. Cadenas E, Davies KJ. Mitochondrial free radical generation, oxidative stress, and aging. *Free Radic Biol Med.* 2000; 29:222–230. [PubMed: 11035250]
48. Nicholls, DG.; Ferguson, SJ. *Bioenergetics.* Vol. 3. Academic Press; San Diego, CA: 2002.
49. Van Blerkom J, Cox H, Davis P. Regulatory roles for mitochondria in the peri-implantation mouse blastocyst: possible origins and developmental significance of differential DeltaPsim. *Reproduction.* 2006; 131:961–976. [PubMed: 16672360]
50. Yu M, Zhou Y, Shi Y, Ning L, Yang Y, Wei X, Zhang N, Hao X, Niu R. Reduced mitochondrial DNA copy number is correlated with tumor progression and prognosis in Chinese breast cancer patients. *IUBMB Life.* 2007; 59:450–457. [PubMed: 17654121]
51. Yadava N, Nicholls DG. Spare respiratory capacity rather than oxidative stress regulates glutamate excitotoxicity after partial respiratory inhibition of mitochondrial complex I with rotenone. *J Neurosci.* 2007; 27:7310–7317. [PubMed: 17611283]
52. Okita K, Ichisaka T, Yamanaka S. Generation of germline-competent induced pluripotent stem cells. *Nature.* 2007; 448:313–317. [PubMed: 17554338]
53. Mitsui K, Tokuzawa Y, Itoh H, Segawa K, Murakami M, Takahashi K, Maruyama M, Maeda M, Yamanaka S. The homeoprotein Nanog is required for maintenance of pluripotency in mouse epiblast and ES cells. *Cell.* 2003; 113:631–642. [PubMed: 12787504]
54. Nye HL, Cameron JA, Chernoff EA, Stocum DL. Extending the table of stages of normal development of the axolotl: limb development. *Dev Dyn.* 2003; 226:555–560. [PubMed: 12619140]
55. Belfiore F, Iannello S. Fatty acid synthesis from glutamate in the adipose tissue of normal subjects and obese patients: an enzyme study. *Biochem Mol Med.* 1995; 54:19–25. [PubMed: 7551812]
56. Coles NW, Johnstone RM. Glutamine metabolism in Ehrlich ascites-carcinoma cells. *Biochem J.* 1962; 83:284–291. [PubMed: 13880493]
57. DeBerardinis RJ, Sayed N, Ditsworth D, Thompson CB. Brick by brick: metabolism and tumor cell growth. *Curr Opin Genet Dev.* 2008
58. DeBerardinis RJ, Mancuso A, Daikhin E, Nissim I, Yudkoff M, Wehrli S, Thompson CB. Beyond aerobic glycolysis: transformed cells can engage in glutamine metabolism that exceeds the requirement for protein and nucleotide synthesis. *Proc Natl Acad Sci U S A.* 2007; 104:19345–19350. [PubMed: 18032601]

59. Rosano GM, Vitale C, Sposato B, Mercurio G, Fini M. Trimetazidine improves left ventricular function in diabetic patients with coronary artery disease: a double-blind placebo-controlled study. *Cardiovasc Diabetol.* 2003; 2:16. [PubMed: 14641923]

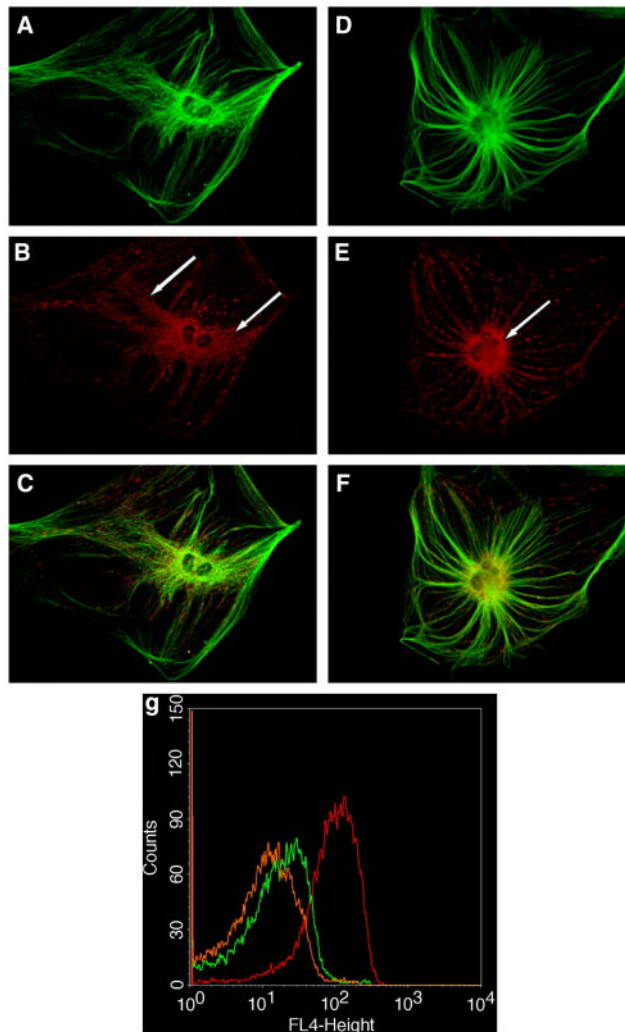


Figure 1. Cytoskeletal Associations and Subcellular Distribution of Mitochondria in MRL and C57BL/6 Fibroblasts

A. C57BL/6 fibroblast microtubules immunostained for α -tubulin. B. C57BL/6 mitochondria localized with Mitotracker Orange CMTMRos. C. Merge of A and B. D. MRL fibroblast microtubules immunostained for α -tubulin. E. MRL mitochondria localized with Mitotracker Orange CMTMRos. F. Merge of D and E. Arrows indicate the cytoplasmically distributed mitochondria in B6 cells that extend to the plasma membrane (B), and the perinuclear mitochondria in MRL cells (E). **Bioenergetic and Biochemical Features. g. Mitochondrial Transmembrane Potential ($\Delta\Psi_m$).** Frequency distributions of $\Delta\Psi_m$ measured by DiIC₁(5) fluorescence (FL4). C57BL/6 fibroblasts (red line), MRL fibroblasts (green), and MRL Day 17 Ear hole blastema cells (orange). **h. Lactate Production in Primary Ear Skin Fibroblasts** was measured in exponentially growing cells under ambient (21%) oxygen. **i. Reactive Oxygen Species (ROS) Production** in Primary Fibroblasts Measured by DHR123 Fluorescence. **Tissue and Cellular Glutathione Content.** j. Liver, k. Heart, l. Primary Ear Skin Fibroblasts.

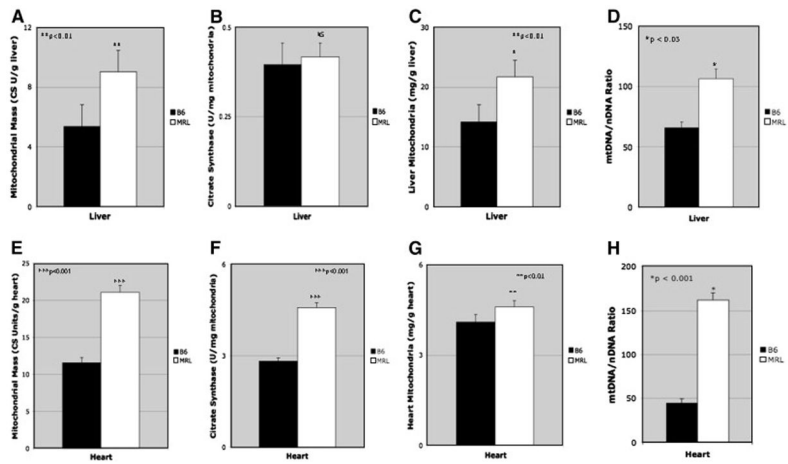


Figure 2. Tissue Mitochondria and Mitochondrial DNA Content

Organ-specific mitochondrial citrate synthase content was measured as an indicator of the total amount of mitochondrial matrix present in liver (A) and heart (E). Mitochondrial matrix packing density was expressed in units of citrate synthase per mg mitochondrial protein (B and F). Tissue-specific total mitochondrial protein content (C and G). Mitochondrial DNA Content was measured by real-time, quantitative PCR (QPCR) and expressed as a ratio of mtDNA to the single-copy nuclear marker SDHa in D. Liver, and H. Heart.

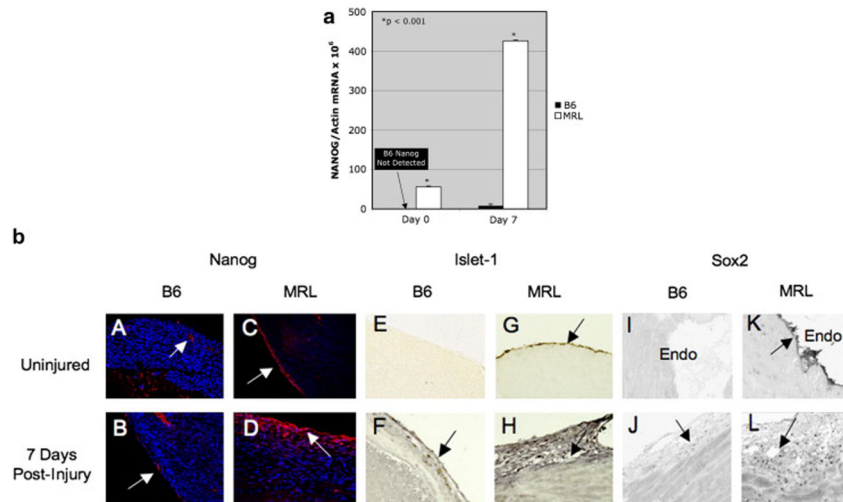


Figure 3. Stem Cell Markers in the Adult MRL Heart

a. Nanog RT-QPCR. Real-time, reverse transcription QPCR was used to measure the abundance of Nanog mRNA relative to β -Actin, before and after cardiac cryoinjury in adult B6 and MRL mice. **b. Immunohistochemistry** Panels A–D are sections stained for Nanog. Arrows indicate areas of expression. Nanog expression was confined to vessel endothelium and the endocardium in the uninjured B6 (A and B). Robust expression was observed in the epicardium of the uninjured MRL heart (C), with increased expression and migration into the myocardium in the injured MRL heart (D). Panels E–H are stained for Islet-1. Panels I–L are stained for Sox2. The epicardium is shown in all sections except in Panels I and K, in which the endocardium is shown. Normal tissues before injury are shown in panels A, C, E, G, I, and K. Injured tissues, 7 days after cryoinjury, are shown in panels B, D, F, H, J, and L.

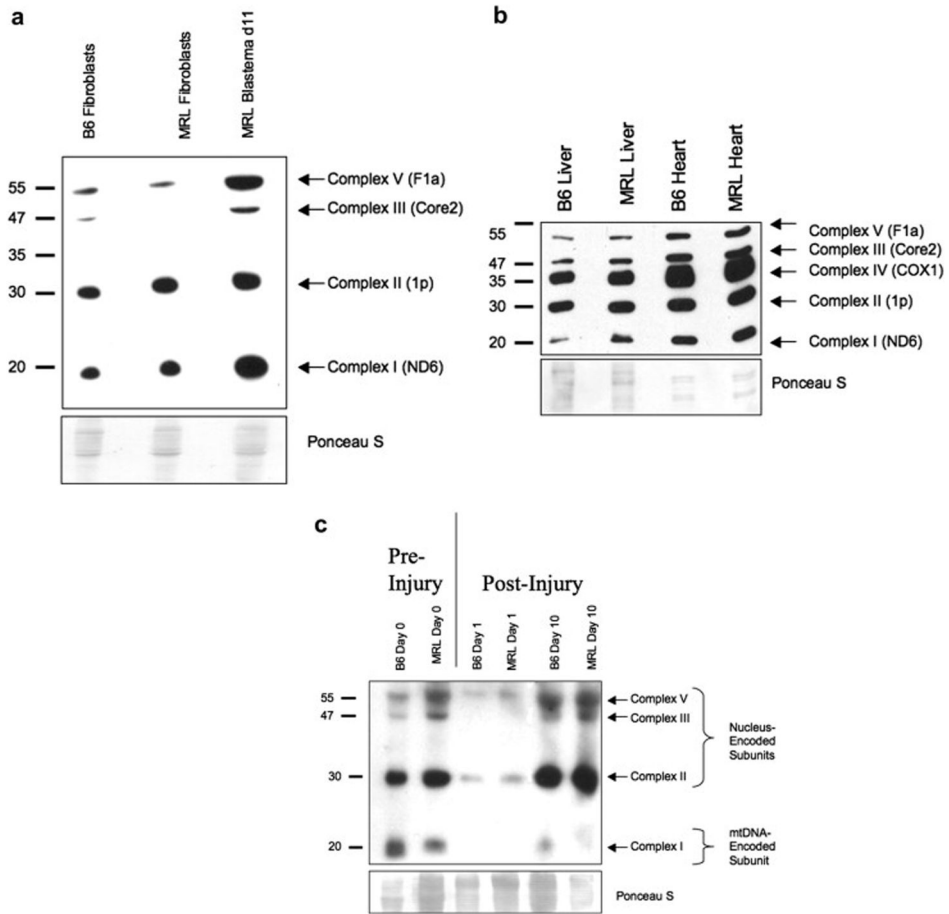


Figure 4. Western Analysis of Mitochondrial Respiratory Chain Subunits was measured in a. Primary Fibroblasts and Day 11 Blastema-derived cells, b. in Isolated Mitochondria from Liver and Heart, and c. in Ear Pinnae before (Day 0), and after ear hole injury on Day 1 and Day 10.

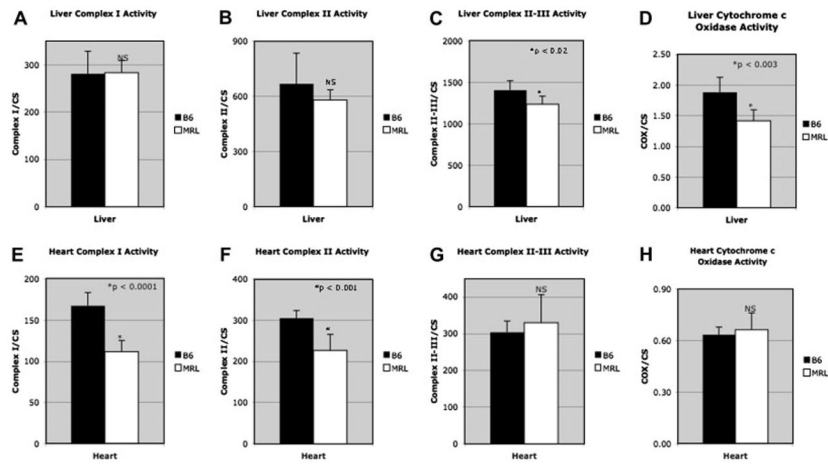


Figure 5. Respiratory Chain Enzymology

A. Liver Complex I, B. Liver Complex II, C. Liver Complex II/III, D. Liver Liver Complex IV (cytochrome c oxidase; COX), E. Heart Complex I, F. Heart Complex II, G. Heart Complex II/III, H. Heart Complex IV (cytochrome c oxidase; COX).

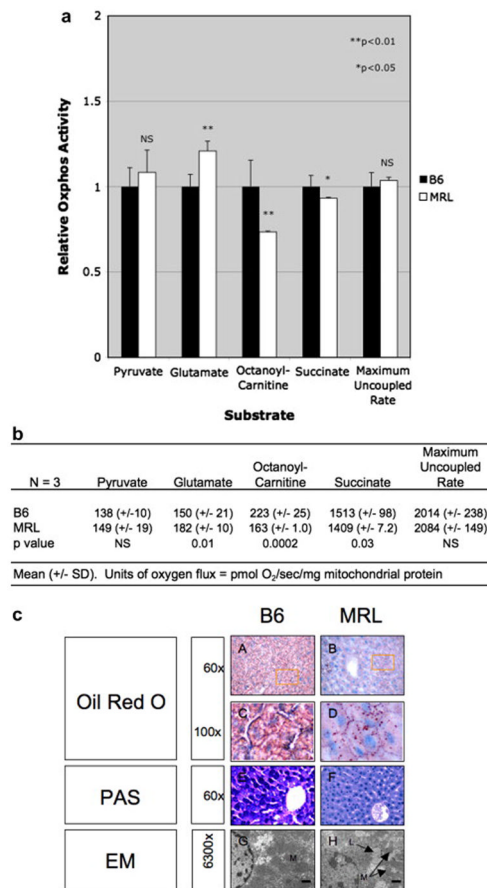


Figure 6. Mitochondrial Oxidative Phosphorylation and Histology

a. Substrate-Specific Respiration of Liver Mitochondria. Values were expressed as a ratio to B6. b. Substrate-Specific oxygen fluxes in pmol/sec/mg. c. **Liver Histology and Ultrastructure.** Frozen sections were stained with oil red O for neutral lipid (A–D), or PAS for glycogen (E–F). Panels C and D are enlargements of the indicated regions from panels A–B. Cellular ultrastructure was evaluated by electron microscopy (EM) in liver from B6 (G), MRL (H) mice. The bar is 1 μ m. (M=mitochondria, L=lipid droplet).